ACCSCIENCE PUBLISHING

Journal of Energy and Sustainability

SHORT COMMUNICATION

Computational fluid dynamics analysis and correlation development for evacuated tube solar air heater with helically roughened tubes

Inderjeet Singh*

Department of Renewable Energy Engineering, Punjab Agricultural University, Ludhiana, Punjab, India

Abstract

In this study, an evacuated tube collector (ETC) solar air heater employing a helical insert (HI) was numerically investigated. The ANSYS Academic Research 16.2 software was used to investigate the effect of geometrical and flow parameters on heat transfer enhancement in an ETC solar air heater roughened with helical inserts (HI's). In the computational fluid dynamics (CFD) analysis, factors P/D_h = 0.5–2, e/D_h = 0.018–0.074, and mass flow rates ranging from 0.003 to 0.015 kg/s were considered. The influence of these factors on thermal and pressure-drop characteristics was examined, and empirical correlations for heat transfer and friction factor were determined using regression analysis.

Keywords: Thermo-hydraulic performance; Heat transfer; Computational fluid dynamics; Evacuated tube collector; Renewable energy

***Corresponding author:**
Inderjeet Singh
(inderjeetsingh.pau@gmail.com)

Citation: Singh I. Computational fluid dynamics analysis and correlation development for evacuated tube solar air heater with helically roughened tubes. *Journal of Energy and Sustainability*. 2025;1(2):025360019. doi: 10.36922/JES025360019

Received: September 1, 2025

Revised: October 30, 2025

Accepted: November 12, 2025

Published online: November 25, 2025

1. Introduction

Solar energy can be effectively utilized for thermal purposes by capturing and transforming it into heat through the use of thermal collectors.[1] There are various kinds of solar collectors available for thermal applications. Technologies that rely on solar energy, such as solar air heaters, solar water heaters, and photovoltaic systems, have been effectively employed in numerous sectors to fulfill energy needs.[2,3] Among the most widely used methods for capturing the thermal component of solar radiation are solar thermal collectors, which absorb radiation energy and convert it into heat.[4] This heat is then used to warm the fluid flowing through the system, which can be applied to space heating, water heating, drying, and agricultural uses.[5] A typical solar thermal collector is composed of glass cover(s), an absorber plate, channels, and insulation.

Solar air heaters, water heaters, and solar dryers are the thermal devices employed for heating air, water, and drying crops, respectively.[6] Solar air heaters are deemed to be more compact and less complicated, and do not encounter corrosion and freezing issues.[2] Furthermore, owing to low-cost fabrication and inherent ease of use, they are user-friendly collection devices for applications such as heating, timber drying, industrial operations, and drying of building components.[7]

The thermal performance of solar air heaters is adversely limited due to low convective heat transfer coefficient between the absorber and the air, which necessitates

design considerations to make them economically viable.[8] In a simple solar air heater, a thin, low heat transfer fluid layer develops near the wall. Heat transfer happens by conduction in this area, and the convection coefficient is very minimal.[9] Thus, the intention is to maximize the heat transfer rate in this region. There are two commonly used techniques of augmenting the heat transfer coefficient. The first approach involves expanding the area using fins or extended surfaces, which adversely affects the pressure drop and is not economically suitable.[10] The second approach involves creating disruption in the downstream region using small obstacles.

For this purpose, introducing artificial roughness on the airflow side of the duct surface is the most economic and valuable method to improve the heat transfer at a little expense of pressure drop.[11] The technique significantly improves the thermal performance and results in a slight increase in frictional losses, leading to higher pumping requirements for the fan or blower. Optimal performance can be achieved by creating turbulence only in the vicinity of the duct surface and using methods such as machining, forming, welding, or fixing roughness elements.[12] Many investigators have attempted to formulate roughness elements in different shapes and arrangements, which can optimally enhance the thermal capability of the system and sustaining the frictional losses to the lowest level.

Solar air heaters are successfully analyzed and optimized using the computational fluid dynamics (CFD) technique for better efficiency and performance enhancement. The outcomes of the numerical investigations are influenced not only by the design or geometrical parameters, but also by the selection of the flow domain, mesh generation, application of boundary conditions, and significantly depend on the turbulence model selected. Although this method has been widely studied in flat plate solar collectors, the influence of turbulence in evacuated tube collectors (ETCs) remains underexplored. Very few CFD studies on ETC solar air heaters have been conducted to evaluate the detailed flow phenomena inside the solar air heaters and their statistical correlation with parameters. Thus, the present work aims to depict the thermal and hydraulic performance of an ETC solar air heater using a novel helically roughened solar vacuum tube for heat transfer enhancement.

2. Material and methods

In the numerical analysis, a three-dimensional (3D) domain was constructed using ANSYS academic research software (ANSYS Inc., USA). To curtail the computational effort, the inner coaxial pipes directing the flow in the tube were excluded from the domain. Helical inserts (HIs) were modeled on the airflow side. These inserts were examined in different configurations by altering the coil pitch-to-diameter ratio (P/D_h), height ratio (e/D_h), and mass flow rate.[13,14] The numerical and experimental results that are reported in this study have been published in the author's previous article.[15]

2.1. Meshing

The 3D flow field was divided into tetrahedral cells using ANSYS Meshing, as depicted in Figure 1. To achieve higher accuracy and maintain a y+ value below 1, a much finer grid was created near the absorber wall.[16-18] A grid independence check was conducted using the gradient adaption method to verify the numerical simulation's accuracy. A grid system with 2,352,160 cells was deemed sufficiently fine for further investigation.

2.2. Governing equations

Several governing equations are listed in the following:

Continuity equation:

$$\nabla.(\rho.\vec{v}\ ) = 0 \tag{1}$$

Momentum equation:

$$\nabla.(\rho.\vec{v}\ .\vec{v}) = -\nabla p + \nabla.\left(\mu\left[\left(\nabla\vec{v} + \nabla\vec{v}^{T}\right) - \frac{2}{3}\nabla.\vec{v}I\right]\right) \tag{2}$$

Energy equation:

$$\nabla.\left(\vec{V}\left(\rho E + p\right)\right) = \nabla.(k_{eff}\nabla T - h\vec{J} + \left(\mu\left[\left(\nabla\vec{\upsilon} + \nabla\vec{v}^{T}\right) - \frac{2}{3}\nabla.\vec{v}I\right].\vec{\upsilon}\right) \tag{3}$$

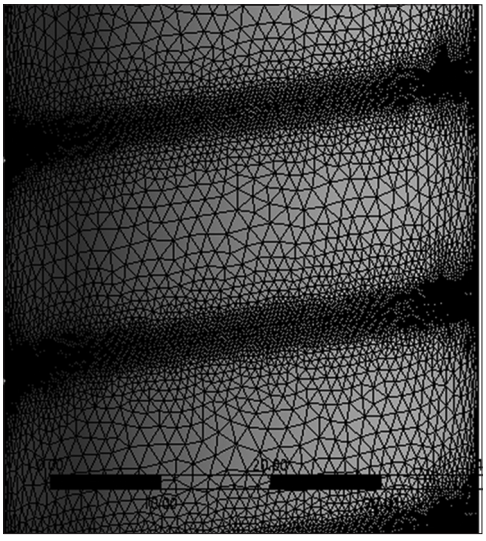

Figure 1. Grid generated on the flow domain of a helical coiled solar air heater

2.3. Methodology

For the numerical calculations, the RNG K-epsilon (k-ε) turbulence model[19] with enhanced wall treatment (EWT) was employed to analyze the flow characteristics within the tubes. The simulation utilized a double-precision SIMPLE algorithm for coupling velocity and pressure, while a second-order upwind scheme was applied for term discretization. The convergence criteria were set at 10^{-5} for flow equations and 10^{-10} for the energy equation.

To replicate the airflow, a mass flow rate condition was applied at the inlet boundary using air at a temperature of 300 K, which exists as a fluid. The other walls were subjected to no-slip conditions. A uniform heat flux of 1000 W/m^2 was applied to the tube surface. The air's thermo-physical properties were taken as constant based on the preliminary study showing no significant difference in the Nusselt number outcome. The simulation assumes steady-state circumstances and incompressible flow. Throughout the iterations, the convergence of residuals was monitored, and the Nusselt number was noted.

3. Results and discussion

Figure 2 depicts the influence of mass flow rate on heat transfer investigated at different P/D_h values. To accomplish this investigation, the height ratio (e/D_h) has been kept fixed at 0.074. For comparison, results include the Nusselt number for the plain tube ETC solar air heater. As anticipated, the Nusselt number consistently increased with a rise in mass flow rate for both the modified and simple ETCs. The peak was achieved at a mass flow rate of 0.015 kg/s when P/D_h was 1.5. This implies the optimum pitch is required for achieving maximum local heat transfer rate by optimizing the distance between two turbulence-creating objects. This phenomenon is due to the reduction in the recirculation area behind the HI, as depicted in Figure 3, which is associated with low heat transfer. In addition, at elevated mass flow rates, the intensity of turbulence also rises in that area. Collectively, both effects mark the reason behind the monotonically increasing trend of the Nusselt number.

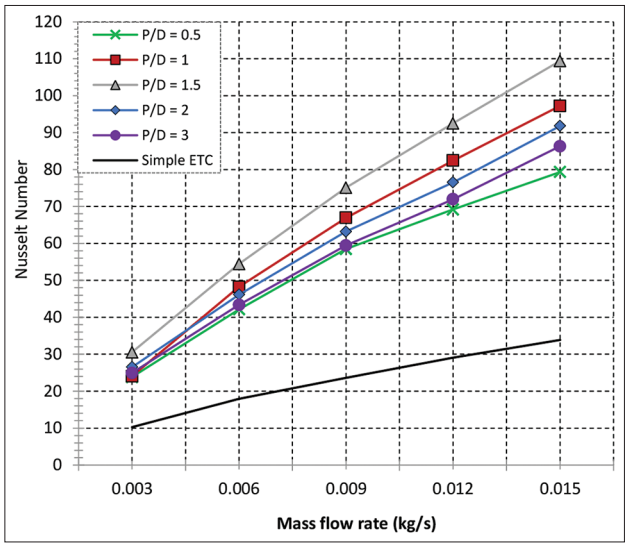

Figure 2. Influence of mass flow rate on Nusselt number characteristics at different P/D_h values
Abbreviation: ETC: Evacuated tube collector.

Figure 3A-C illustrates the influence of airflow rate and flow structure, describing the thermal attributes at different mass flow rates. Figure 3A clearly shows that at a mass flow rate of 0.003 kg/s, the reattachment happens after quite a large distance, and this area before reattachment exhibits a low heat transfer coefficient. Thus, the Nusselt number at a lower mass flow rate is less. However, on increasing the airflow rate, the reattachment points shift closer by 8.57% to the coiled insert, and the low heat transfer zone gets reduced, and consequently, the Nusselt number is increased. On further increasing the mass flow rate to 0.015 kg/s, this zone gets significantly reduced by 20.3% (Figure 3C), and more area between the two coils possesses

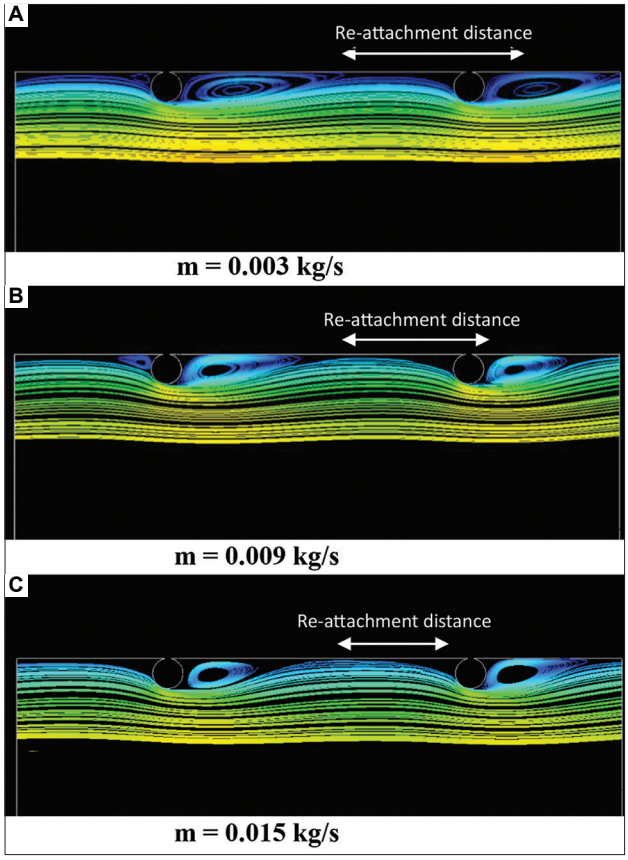

Figure 3. Variation of flow pattern inside the evacuated tube collector (ETC) solar air heater with mass flow rate

a higher local heat transfer coefficient. Thus, the Nusselt number monotonically moves upward with increasing the mass flow rate from 0.003 to 0.015 kg/s.

Figure 4 illustrates the contours of turbulent intensity for ETC-HI at various P/D_h ratios at m = 0.015 kg/s. Turbulent intensity reflects the improved heat transfer mechanism due to increased particle movement, which enhances heat and momentum transport. Greater turbulent intensity also results in improved flow mixing. Consequently, it represents the heat transfer characteristics observed in different cases studied for the ETC-HI solar air heater. An improvement of the turbulence intensity was visually observed after insertion of the helical coil, which suggests an increase in particle movement and flow mixing, thus boosting the heat transfer. This is in contrast to the conventional tube collector, where turbulence intensity remains low. The helical coiled insert exhibits significantly higher intensity of turbulence levels, leading to an increased Nusselt number compared to the smooth tube collector.

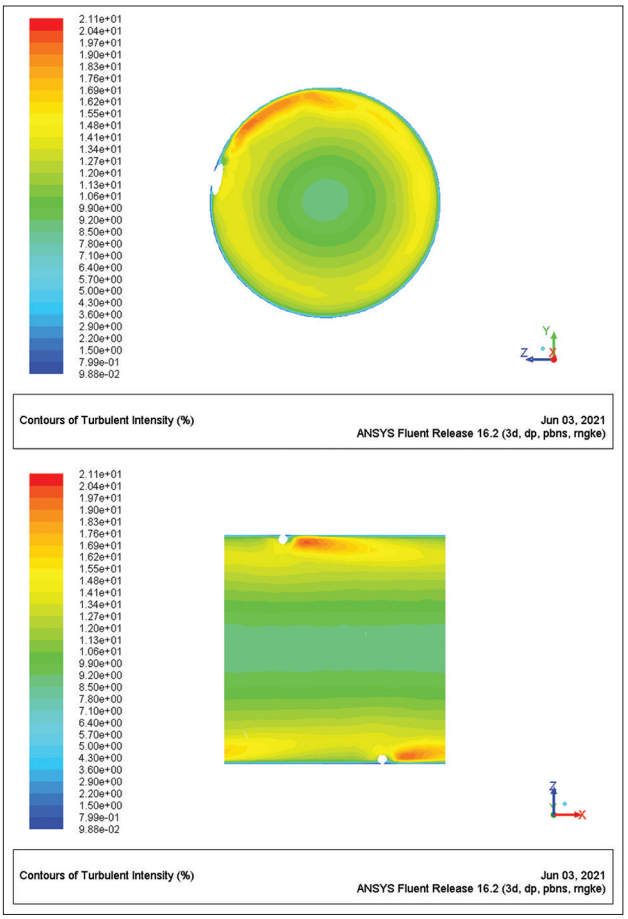

Figure 4. Turbulence intensity contours for evacuated tube collector with helical insert (ETC-HI) at different P/D_h =1.5. Top panel: Cross-sectional view; Bottom panel: Side view.

The peak turbulence intensity of 27.7% was obtained for P/D_h = 1.5, indicating the optimal pitch value and aligning with the highest Nusselt number achieved at this value. A similar trend in the Nusselt number was observed for all pitch values, although the scale values differed in all the cases investigated.

Figure 5 depicts the contours of the surface Nusselt number inside the vacuum tubes equipped with HIs. The amplification of the Nusselt number can be visualized due to periodic obstacles to the airflow, hence disrupting the laminar sub-layer. Nusselt number is significantly amplified in the vicinity of the rib in the downstream area where the flow reattachment takes place. Compared to the smooth duct, a Nusselt number enhancement of 3.6 times was observed, as indicated by the corresponding values.

Figure 6 illustrates the Nusselt number changes with varying height ratios (e/D_h) from 0.018 to 0.074, scrutinized at different mass flow rates. It is evident that the height of the coil wire produces a substantial effect on the Nusselt number. Within the studied range of height ratio, the Nusselt number consistently rose until the e/D_h reached the value of 0.074. A similar trend was observed across other mass flow rates. For every e/D_h value investigated in the study, the heat transfer in ETC-HI is notably amplified compared to a plain ETC.

3.1. Pressure drop characteristics

The introduction of helical obstacles to the airflow leads to a disruption in flow, resulting in a greater pressure drop, which in turn increases the friction factor. Besides the obstruction, the enhanced flow mixing and turbulence also contribute to a notable pressure drop, thereby affecting the friction factor. Consequently, the impact of helical coiled

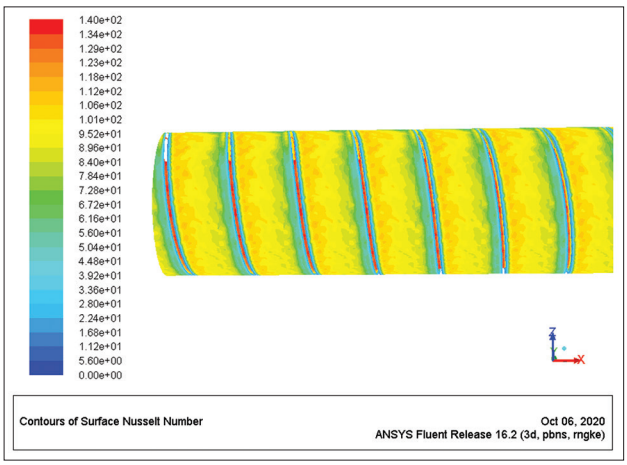

Figure 5. Surface Nusselt number contours on the evacuated tube collector with helical inserts (ETC-HI)

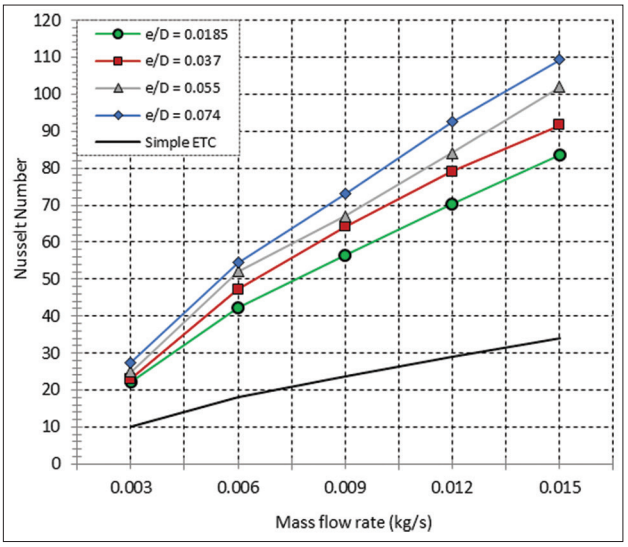

Figure 6. Nusselt number variation at different height ratios (e/D_h)
Abbreviation: ETC: Evacuated tube collector.

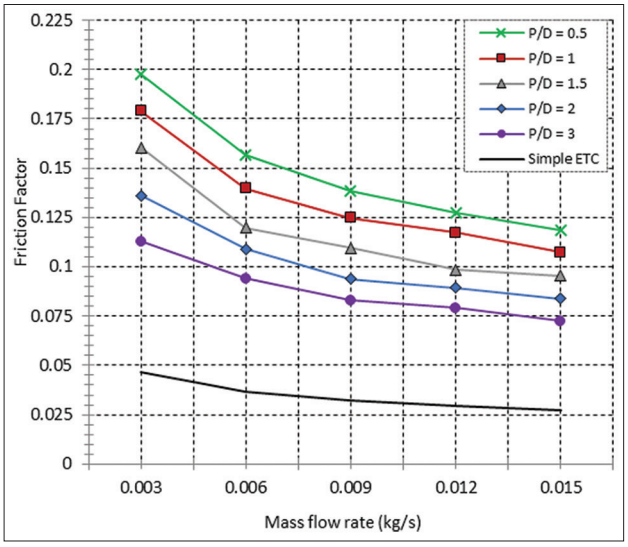

Figure 7. Friction factor trend variation for various pitch ratios at different mass flow rates
Abbreviation: ETC: Evacuated tube collector.

inserts on friction factor characteristics was assessed using the Darcy–Weisbach equation as follows:

$$f = \frac{2(\Delta P)_d D_h}{4\rho L v^2} \quad (4)$$

Figure 7 illustrates how mass flow rate influences pressure drop and subsequently the friction factor of the modified ETC-HI solar air heater. Comparative data of the plain ETC is also presented for reference comparison. In general, the friction factor declines with increasing mass flow rate across all examined parameters, even though the pressure losses show an upward trend. The highest friction factor is observed at a m = 0.003 kg/s, and the lowest corresponds to m = 0.015 kg/s. This pattern is noted for other helical pitch ratios. The influence of coiled inserts is most pronounced at m = 0.003 kg/s, conforming to P/D_h = 0.5, due to a higher number of obstacles along the tube length. It is also noteworthy that a significantly higher friction factor is observed across all examined parameters, highlighting the frictional penalty associated with improved heat transfer using coiled inserts.

Figure 8 illustrates the influence of coil wire diameter on the friction factor. Conclusively, it is clear that the friction factor consistently upsurges as the diameter of the coil wire is increased. The highest friction factor values are asrociated with an e/D_h = 0.074, corresponding to the 2 mm obstacle height. As the e/D_h ratio decreases to 0.018, the trend shows a consistent decline.

In the present study, the maximum Nusselt number enhancement of 3.23 times was observed, whereas the

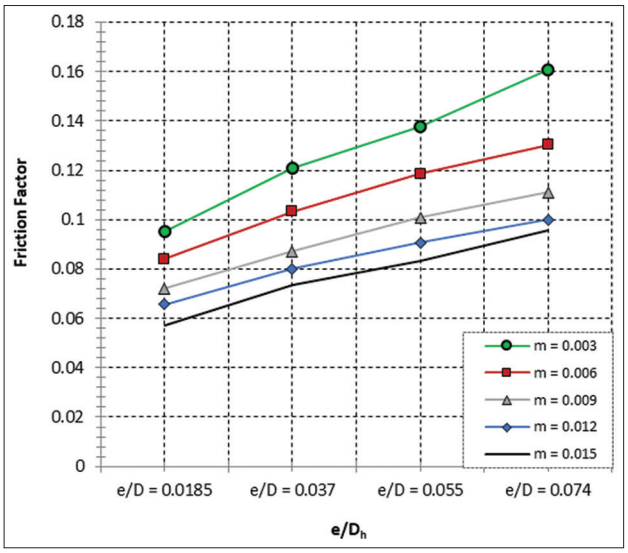

Figure 8. Friction factor for evacuated tube collector with helical insert (ETC-HI) for the investigated e/D_h values

friction factor penalty was found to be 4.36 times. The thermohydraulic performance parameter varied from 1.43 to 2.13, indicating the significant benefit of creating turbulence in ETC. The peak value of 2.13 was obtained for the HIs, showing a significant improvement in contrast to the thermohydraulic performance parameter of 1.36 reported for circular ribs by Singla *et al.*[16] This might be attributed to the lesser pressure drop associated with inclined flow structure, coupled with more heat transfer augmentation, resulting in a higher thermohydraulic performance parameter.

3.2. Statistical correlation

Based on the exploration of ETC with helical coiled inserts, it is apparent that considerable improvement in thermal performance has been attained. Alongside this enhancement, there is a significant penalty in the friction factor. It is evident that both are strong functions of the obstacle parameters. The correlations between Nusselt number and friction factor have been analyzed using regression analysis to calculate their functional relationship.[20] Their functional relationship with various influencing factors is defined as follows:

$$Nu = f_n\,(Re, P/D, e/D) \tag{5}$$

$$f = f_n\,(Re, P/D, e/D) \tag{6}$$

The initial step involves establishing the statistical correlation between the Nusselt number and the Reynolds number. The data points for the Nusselt number, corresponding to the Reynolds number, were represented on a log-log scale for different roughness parameters (Figure 9). The curve fitting using the least square fit indicates a linear relationship with Reynolds number. Therefore, the functional relationship between these can be expressed as:

$$Nu = A_0\,Re^{0.8097} \tag{7}$$

A_0 is a function of coil pitch ratio (P/D_h) and height ratio (e/D_h). Considering P/D_h, the value of $Nu/Re^{0.8097} = A_o$ is plotted against P/D_h. Regression curve fitting is shown in Figure 10 and may be represented by:

$$\frac{Nu}{Re^{0.8097}} = B_0 \left(\frac{P}{D}\right)^{0.116}\left[exp(-0.2226)\,ln\left(\frac{P}{D}\right)^2\right] \tag{8}$$

The constant B_0 is further dependent on e/D_h and can be expressed as:

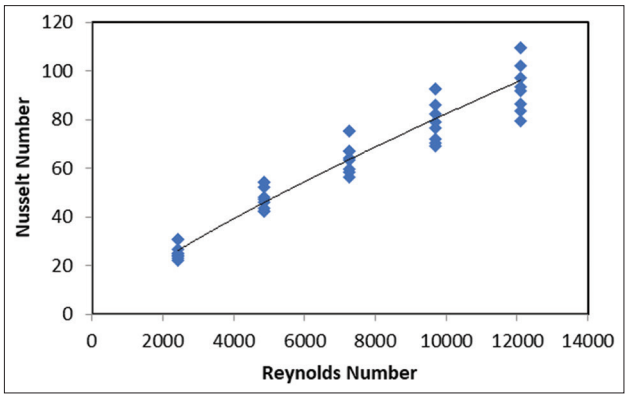

Figure 9. Plot of Nusselt number versus Reynolds number for all data points

$$B_o = \frac{\dfrac{Nu}{Re^{0.8097}}}{\left(\dfrac{P}{D}\right)^{0.116}\left[exp(-0.2226)\,ln\left(\dfrac{P}{D}\right)^2\right]} \tag{9}$$

Finally, the relationship between B_o and e/D_h is plotted in Figure 11. A quadratic fit is obtained as follows:

$$\frac{\dfrac{Nu}{Re^{0.8097}}}{\left(\dfrac{P}{D}\right)^{0.116}\left[exp(-0.2226)\,ln\left(\dfrac{P}{D}\right)^2\right]} = C_o\left(\frac{e}{D}\right)^{0.7874}\left[exp(0.0892)\,ln\left(\frac{e}{D}\right)^2\right] \tag{10}$$

Finally, rearranging the above equation and evaluating C_o, the statistical correlation is obtained as follows:

$$Nu = 0.2364\,Re^{0.8097}\left(\frac{P}{D}\right)^{0.116} \times\left[exp(-0.2226)\,ln\left(\frac{P}{D}\right)^2\right] \times\left(\frac{e}{D}\right)^{0.7874}\left[exp(0.0892)\,ln\left(\frac{e}{D}\right)^2\right] \tag{11}$$

A similar method was employed to establish a correlation for the friction factor (Figures 12-14). The final correlation is expressed as:

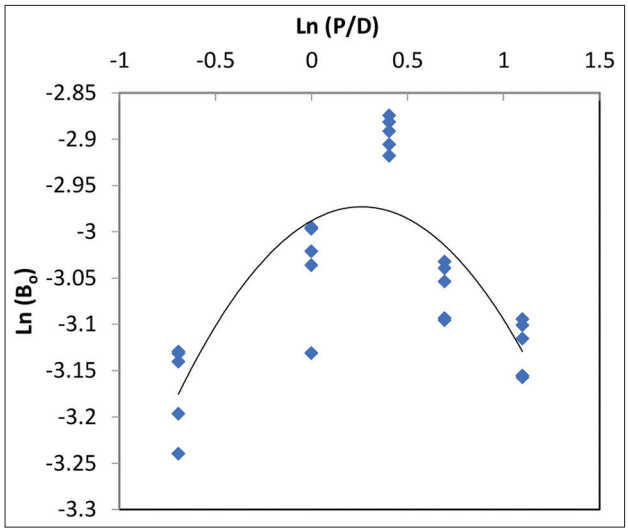

Figure 10. Plot of Ln ($Nu/Re^{0.8097}$) as a function of Ln (P/D)

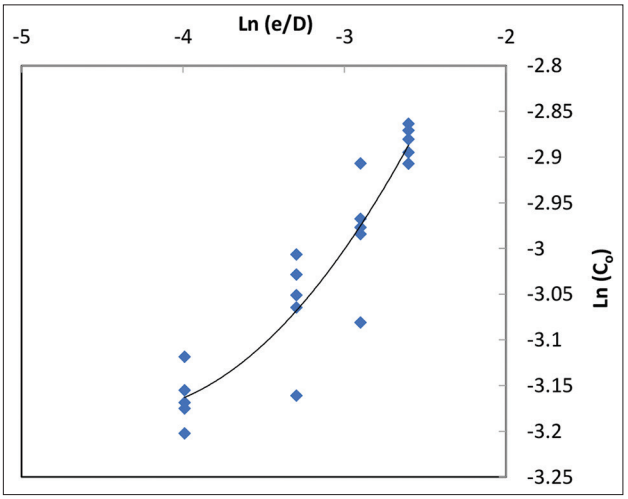

Figure 11. Plot of Ln (Nu/Re$^{0.8097}$ (P/D)$^{0.116}$ exp (-0.2226) ln(P/D)^2) as a function of Ln (e/D)

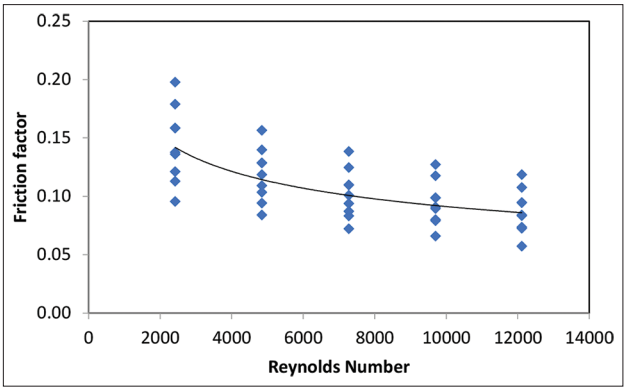

Figure 12. Plot of friction factor versus Reynolds number for all data points

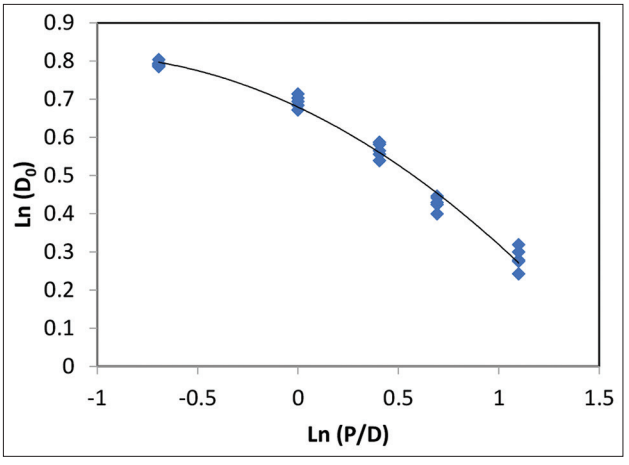

Figure 13. Plot of Ln (f/Re$^{-0.311}$) as a function of Ln (P/D)

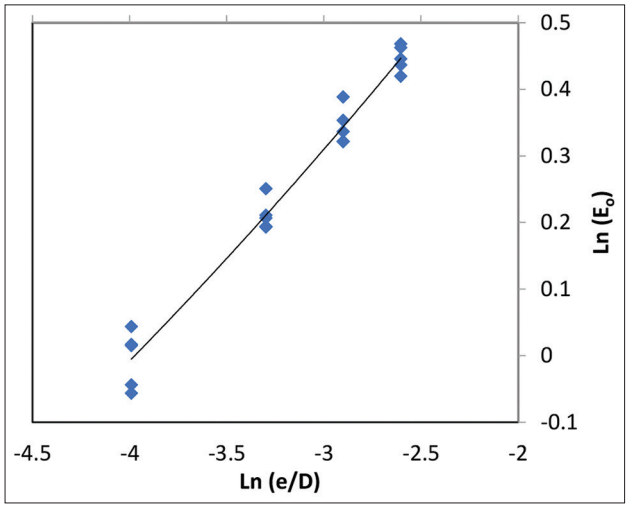

Figure 14. Plot of Ln (Nu/Re$^{-0.311}$ (P/D)$^{-0.2475}$ exp (-0.1127) ln(P/D)^2) as a function of Ln (e/D)

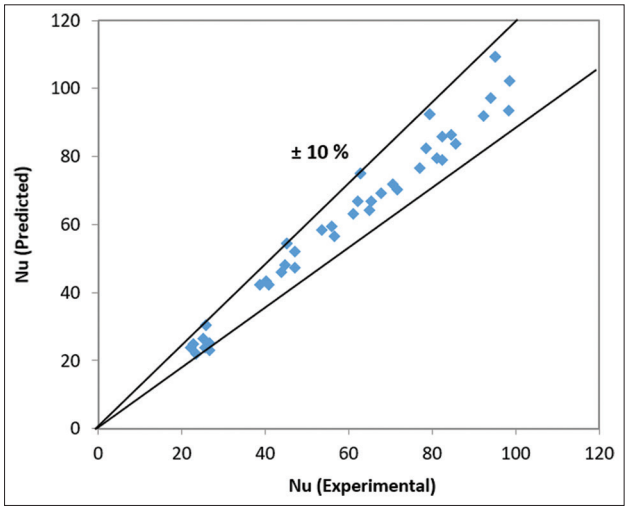

Figure 15. Comparison of predicted and experimental Nusselt number (Nu) values

$$f = 4.472\,Re^{-0.311}\left(\frac{P}{D}\right)^{-0.2475} \times\left[exp\left(-0.1127\right)ln\left(\frac{P}{D}\right)^{2}\right] \times\left(\frac{e}{D}\right)^{0.455366}\left[exp\left(0.0196\right)ln\left(\frac{e}{D}\right)^{2}\right] \quad (12)$$

Figures 15 and 16 illustrate the comparison between experimental results and those predicted using the developed correlation for the Nusselt number and friction

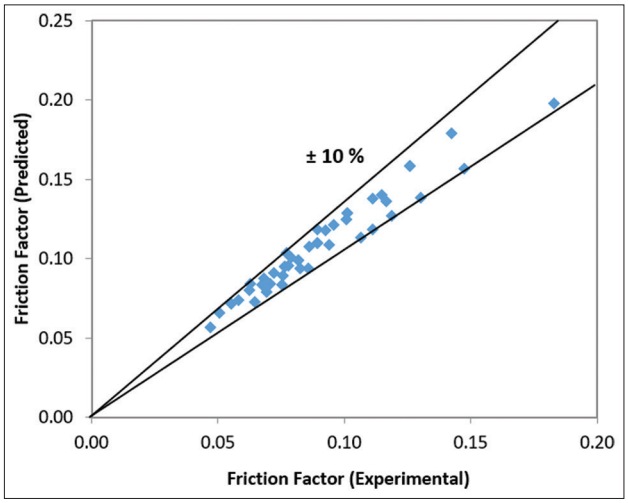

Figure 16. Comparison of predicted and experimental values of the friction factor

factor, respectively. Approximately 96% of the predicted data falls within ±10% of the experimentally observed values. The regression analysis for the correlation yields a regression coefficient of 0.97. Consequently, the developed correlations can accurately predict the Nusselt number and friction factor within the investigated parameter range.

4. Conclusion

In this investigation, a numerical study of a modified vacuum tube solar air heater employing helical coils was conducted using the ANSYS Academic Research 16.2 software to analyze the effect of geometrical and flow parameters on thermal performance enhancement. In the CFD analysis, parameters $P/D_h = 0.5–2$, $e/D_h = 0.018$-0.074, and mass flow rates ranging from 0.003 to 0.015 kg/s were considered. The findings were visualized using graphical contours and streamlines for various cases. The maximum heat transfer augmentation of 3.2 times was observed in the ETC roughened with helical coils, compared to the conventional ETC solar air heater, corresponding to $P/D_h = 1.5$, $e/D_h = 0.074$, and at m = 0.015 kg/s. The thermohydraulic performance parameter of the modified collector improves from 1.43 to 2.13, indicating the significant benefit of creating turbulence in ETC. Nusselt number and friction factor correlations are determined by performing regression analysis, which can be expressed as follows:

$$Nu = 0.2364\,Re^{0.8097}\left(\frac{P}{D}\right)^{0.116} \times\left[exp\left(-0.2226\right)ln\left(\frac{P}{D}\right)^{2}\right] \times\left(\frac{e}{D}\right)^{0.7874}\left[exp\left(0.0892\right)ln\left(\frac{e}{D}\right)^{2}\right] \quad (13)$$

$$f = 4.472\,Re^{-0.311}\left(\frac{P}{D}\right)^{-0.2475} \times\left[exp\left(-0.1127\right)ln\left(\frac{P}{D}\right)^{2}\right] \times\left(\frac{e}{D}\right)^{0.455366}\left[exp\left(0.0196\right)ln\left(\frac{e}{D}\right)^{2}\right] \quad (14)$$

Acknowledgments

None.

Funding

None.

Conflict of interest

The author declares no conflict of interest.

Author contributions

This is a single-authored article.

Ethics approval and consent to participate

Not applicable.

Consent for publication

Not applicable.

Availability of data

Data are available from the corresponding author upon reasonable request.

References

1. Kalogirou SA. Solar thermal collectors and applications. *Prog Energy Combust Sci*. 2004;30(3):231-295.

   doi: 10.1016/j.pecs.2004.02.001

2. Kabeel AE, Hamed MH, Omara ZM, Kandeal AW. Solar air heaters: Design configurations, improvement methods and applications - a detailed review. *Renew Sustain Ener Rev*. 2017;70:1189-1206.

   doi: 10.1016/J.RSER.2016.12.021

3. Faisal Ahmed S, Khalid M, Vaka M, *et al*. Recent progress in solar water heaters and solar collectors: A comprehensive review. *Therm Sci Eng Prog*. 2021;25:100981.

   doi: 10.1016/J.TSEP.2021.100981

4. Sukhatme SP, Nayak JK. *Solar Energy*. 4th ed. United States: McGraw Hill Education; 2017.

5. Gorjian S, Calise F, Kant K, *et al*. A review on opportunities for implementation of solar energy technologies in

agricultural greenhouses. *J Clean Prod*. 2021;285:124807.

doi: 10.1016/J.JCLEPRO.2020.124807

6. Kabir E, Kumar P, Kumar S, Adelodun AA, Kim KH. Solar energy: Potential and future prospects. *Renew Sustain Energy Rev*. 2018;82:894-900.

doi: 10.1016/j.rser.2017.09.094

7. Bhushan B, Singh R. A review on methodology of artificial roughness used in duct of solar air heaters. *Energy*. 2010;35(1):202-212.

doi: 10.1016/J.ENERGY.2009.09.010

8. Singh Bisht V, Kumar Patil A, Gupta A. Review and performance evaluation of roughened solar air heaters. *Renew Sustain Enerey Rev*. 2018;81:954-977.

doi: 10.1016/J.RSER.2017.08.036

9. Gill RS, Hans VS, Saini JS, Singh S. Investigation on performance enhancement due to staggered piece in a broken arc rib roughened solar air heater duct. *Renew Energy*. 2017;104:148-162.

doi: 10.1016/J.RENENE.2016.12.002

10. Singh I, Singh S, Vardhan S. Heat transfer and fluid flow characteristics of solar air heater duct with non-uniform ribs. *J Mech Sci Technol*. 2021;35(1):343-350.

doi: 10.1007/s12206-020-1234-9

11. Sharma SK, Kalamkar VR. Thermo-hydraulic performance analysis of solar air heaters having artificial roughness-a review. *Renew Sustain Energy Rev*. 2015;41:413-435.

doi: 10.1016/J.RSER.2014.08.051

12. Alam T, Kim MH. A critical review on artificial roughness provided in rectangular solar air heater duct. *Renew Sustain Energy Rev*. 2017;69(2016):387-400.

doi: 10.1016/j.rser.2016.11.192

13. Yadav AS, Bhagoria JL. A CFD based thermo-hydraulic performance analysis of an artificially roughened solar air heater having equilateral triangular sectioned rib roughness on the absorber plate. *Int J Heat Mass Transf*. 2014;70:1016-1039.

doi: 10.1016/J.IJHEATMASSTRANSFER.2013.11.074

14. Yadav AS, Bhagoria JL. A numerical investigation of square sectioned transverse rib roughened solar air heater. *Int J Ther Sci*. 2014;79:111-131.

doi: 10.1016/J.IJTHERMALSCI.2014.01.008

15. Singh I, Vardhan S. Experimental investigation of an evacuated tube collector solar air heater with helical inserts. *Renew Energy*. 2021;163:1963-1972.

doi: 10.1016/j.renene.2020.10.114

16. Yadav S, Kaushal M, Varun S. Nusselt number and friction factor correlations for solar air heater duct having protrusions as roughness elements on absorber plate. *Exp Therm Fluid Sci*. 2013;44:34-41.

doi: 10.1016/J.EXPTHERMFLUSCI.2012.05.011

17. Karmare SV, Tikekar AN. Analysis of fluid flow and heat transfer in a rib grit roughened surface solar air heater using CFD. *Solar Energy*. 2010;84(3):409-417.

doi: 10.1016/J.SOLENER.2009.12.011

18. Gawande VB, Dhoble AS, Zodpe DB, Chamoli S. Experimental and CFD-based thermal performance prediction of solar air heater provided with chamfered square rib as artificial roughness. *J Brazil Soc Mech Sci Eng*. 2015;38(2):643-663.

doi: 10.1007/S40430-015-0402-9

19. Singla M, Hans VS, Singh S. CFD analysis of rib roughened solar evacuated tube collector for air heating. *Renew Energy*. 2022;183:78-89.

doi: 10.1016/J.RENENE.2021.10.055

20. Saini SK, Saini RP. Development of correlations for Nusselt number and friction factor for solar air heater with roughened duct having arc-shaped wire as artificial roughness. *Solar Energy*. 2008;82(12):1118-1130.

doi: 10.1016/J.SOLENER.2008.05.010